International Journal of Fatigue 168 (2023) 107381

Contents lists available at ScienceDirect

International Journal of Fatigue

journal homepage: www.elsevier.com/locate/ijfatigue

Creep-fatigue of P92 in service-like tests with combined stress- and strain-controlled dwell times

Nadja Sonntag, Maria Jürgens, Birgit Skrotzki, Jürgen Olbricht *

Bundesanstalt für Materialforschung und -prüfung (BAM), Division 5.2: Experimental and Model Based Mechanical Behaviour of Materials, 12205 Berlin, Germany

ARTICLE INFO

Keywords:
Tempered martensite-ferritic steel
P92
Dwell periods
Creep-fatigue interaction
Stress relaxation

ABSTRACT

Complex service-like relaxation- and creep-fatigue tests with strain- and stress-controlled dwells and fatigue cycle durations of approx. 2200 s were performed exemplarily on a grade P92 steel at 620 °C in this study. The results indicate deviations in the prevailing creep mechanisms of long-term relaxation and creep dwells, affecting subsequent dwells, load shifts, and the macroscopic softening behavior quite differently. In addition, fracture surfaces and longitudinal metallographic sections reveal intergranular crack growth for complex loading with *stress-controlled* dwells, whereas complex *strain-controlled* tests enhance oxidation and transgranular crack propagation. These findings substantiate the limited transferability of relaxation-fatigue to creep-fatigue conditions.

* used as abbreviation in text and also as specifying index with symbols.

1. Introduction

Creep-fatigue interactions occur in many safety-relevant components made of high-temperature metallic alloys, in which quasi-static and transient load shifts alternate or overlap. Since they often significantly reduce both fatigue and creep strengths, creep-fatigue testing is an integral part of the mechanical characterization of high-temperature structural materials. Drawing on experience in high-temperature fatigue testing – even low mechanical load amplitudes often cause plastic deformation at high temperature, accompanied by strain-dominated damage – strain-controlled testing has been established for standard creep-fatigue experiments. This usually involves keeping the strain constant for a few seconds to minutes when the minimum or maximum strain in the cycle is reached so that the mechanical stress relaxes as a function of load level and time. Although this procedure is experimentally very practicable and physically justified for high strain amplitudes and short dwell times, it does not adequately represent the actual load situation of components used, e.g., in the energy sector. Instead of predominant fatigue with short phases of constant load, long (stress-controlled) quasi-static loads with occasional fatigue loading due to load shifts are often expected in real components.

Tempered martensite ferritic steels are widely used in components, e.g., boilers, pipes, and superheaters of fossil-fired thermal power plants subjected to high temperatures, creep loading, and hydrogen- or flue gas-containing atmospheres [1]. While these 9–12 %-Cr steels offer an appreciable creep strength and oxidation resistance at elevated temperatures, they are much more cost-effective in terms of alloy costs than Ni-base alloys. Besides, they offer a lower coefficient of thermal expansion and higher thermal conductivity than austenitic stainless steels [2].

9–12 % Cr steels owe their excellent creep properties to their tempered martensitic microstructure: It is characterized by fine grains (former laths) arranged hierarchically in blocks and packets within prior austenite grains [3–5]. Though many dislocations resulting from martensitic transformation annihilate and partially rearrange into subgrain boundaries during tempering, 9–12 % Cr steels initially possess high dislocation densities [6]. Fine, homogeneously distributed MX-type carbonitrides partially pin these dislocations and consequently impede plastic deformation; grain boundary sliding is inhibited by coarser $M_{23}C_6$-type carbides stabilizing the low- and high-angle grain boundaries [7,8].

However, due to fundamental changes in the operating profiles of power plants in the context of the energy transition, these materials, whose properties were once tailored to a high static creep resistance [1,9], are now subjected to cyclic loading: Conventional power plants must react with increasing flexibility to fluctuating feed-in of electricity from renewable energy sources into the power grid. As a result, the number of start-ups, shutdowns, and load shifts per annum has increased continuously in recent years. Especially in the case of thick-walled

* Corresponding author.
E-mail address: juergen.olbricht@bam.de (J. Olbricht).

https://doi.org/10.1016/j.ijfatigue.2022.107381
Received 27 June 2022; Received in revised form 14 October 2022; Accepted 6 November 2022
Available online 11 November 2022

Nomenclature

DT*	dwell time
SLC*	service-like creep
SLR*	service-like relaxation
SSO*	30-min DT emulating a phase of steady-state operation
E	bulk elastic modulus
$\varepsilon = \varepsilon_t$	(total) strain
$\dot{\varepsilon}$	(total) strain rate
$\varepsilon_a = \varepsilon_{t,a}$	total strain amplitude
ε_c	creep strain
$\varepsilon_{start} = \varepsilon_0$	strain at the beginning of a DT
ε_{stop}	strain at the end of a DT
ε_{el}	elastic strain
ε_{min}, ε_{max}	peak strains
$\varepsilon_{pl,i}$	initial plastic strain
G	bulk shear modulus
N_f	fatigue life
ν	Poisson's ratio
R	strain ratio
R_z	surface roughness
σ	stress
σ_{start}	stress at the beginning of a DT
σ_{stop}	stress at the end of a DT
σ_{min}, σ_{max}	peak stresses in a cycle
σ_r	stress relaxation during a DT
$\sigma_{r,min}$, $\sigma_{r,max}$	σ_r in DT at ε_{min} and ε_{min}, respectively
σ_s	shear stress
σ_s/G	normalized shear stress
$\Delta\sigma$	stress range
$\Delta\sigma_{cyc}/2$	cyclic yield stress
T	applied temperature
T_m	melting temperature
T/T_m	homologous temperature
t	time, duration

components with internal thermal variations, these transient load periods lead to strongly diverging local load paths and complex loading situations, which include, e.g., different phase angles between temperature and load variation, and high degrees of multiaxiality [10–12]. Therefore, the interest in thorough analyses of the 9–12 % Cr steels' high-temperature (creep) fatigue properties and damage mechanisms under complex loading has risen steadily.

Starting with studies on standard isothermal low-cycle fatigue (LCF) behavior and continuing with investigations on thermomechanical fatigue (TMF) and fatigue with strain-controlled dwell times (isothermal relaxation-fatigue, RF, and thermomechanical relaxation fatigue, RTMF), the applied testing conditions in materials characterizations have successively approached actual power plant operation. Gradual softening [3,13–17] resulting from accelerated recovery processes and coarsening of the subgrain structure [17,18] were found to dominate the microstructural degradation of, e.g., grade P91 and P92 steel under LCF conditions. The LCF lives obey the classical Coffin-Manson-Basquin relationships and decrease with rising test temperature [3,16,19–21]. TMF lives of 9–12 % Cr steels are strongly dependent on the mean temperature, the applied temperature range, and the specific material under investigation [22–25]. Especially for small temperature ranges at high mean temperature or low mechanical strain amplitudes, TMF may reduce the number of cycles to failure compared to LCF [19,23,25–27]. Allowing time-dependent creep/relaxation processes by implementing strain-controlled dwells in the cycle accelerates damage for both isothermal (cf. Fig. 1) [21,28,29] and thermomechanical conditions [23,25,27] significantly. The most remarkable effects of dwell times on the fatigue life occur at low strain amplitudes, which are more closely related to actual power plant operation than higher degrees of deformation [27].

Fatigue tests with dwells aim at investigating the mechanical behavior under combined cyclic and static (creep-) loads, i.e., creep-fatigue interactions, to represent phases of steady-state operation to a certain extent. During the dwell times, strain is usually kept constant in strain-controlled LCF and TMF tests. The associated stress relaxes with time, i. e., it decreases with increasing time. During the relaxation phase, internal stresses are relieved by recovery processes. Directional deformation also occurs due to creep processes induced by internal and external constraints. Total strain is kept constant, but the elastic strain decreases with decreasing stress while the creep strain increases. The associated elementary metallurgical processes include time- and load-dependent inelastic strain formation (dislocation hardening) and competing dynamic recovery (i.e., thermally activated and possibly stress-assisted site exchange processes of lattice defects and impurity atoms).

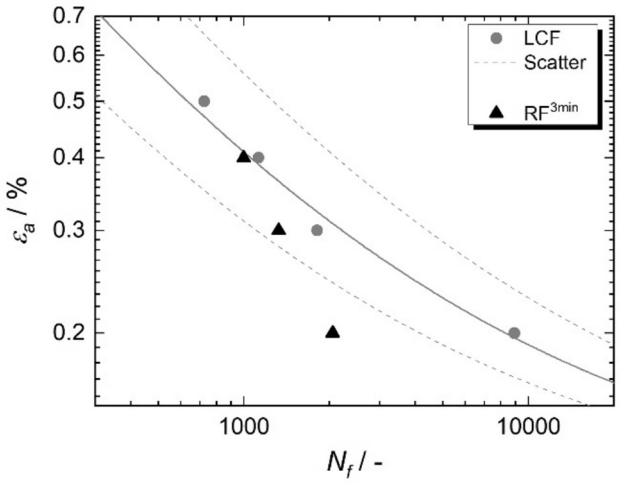

Fig. 1. Fatigue life reduction in relaxation fatigue (RF) tests with symmetrical three-minute dwell periods at ε_{max} and ε_{min} compared to continuous LCF tests of the same P92 material batch as being investigated in this study. Test temperature: 620 °C; strain rate: 1×10^{-3} 1/s; strain ratio, $R = -1$. Lifetime data from [21].

However, these additional periods of static loading increase the cycle (and total test) durations considerably compared to continuous fatigue tests. For this reason, such tests are usually designed and carried out as follows concerning a justifiable time expenditure and ease of handling: (i) the entire test is realized in strain-control, which is common practice in high-temperature fatigue testing, (ii) dwells are introduced for maximum effects at both or one of the peak values ε_{max} and ε_{min} (cf. Fig. 2), (iii) the duration of each dwell (t_{DT}) is chosen in the order of seconds to a few minutes, and (iv) tests with dwells are preferably performed at a high strain amplitude and correspondingly low fatigue life.

This common type of test design is well justified for investigating the damage processes during start-ups, shutdowns, and load shifts with adjusting thermal strains during temperature equilibration in thick-walled tubes. However, since actual power plant operation comprises not only load changes but also still long stress-controlled periods of steady-state operation at low loads in between (in the nominally elastic

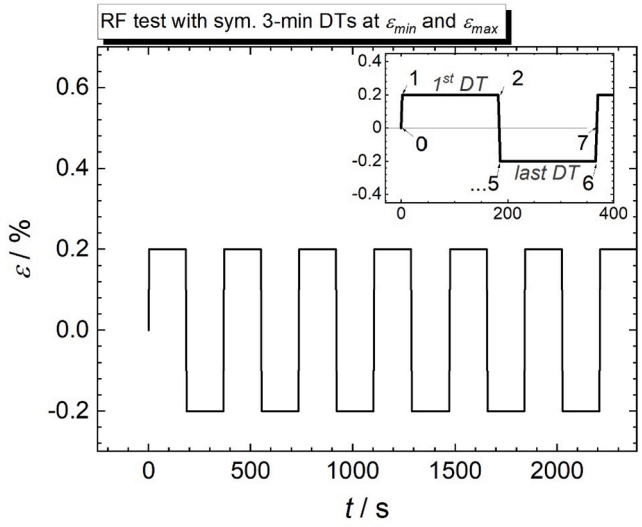

Fig. 2. Typical loading path of an RF test at low strain amplitude and with symmetrical strain-controlled dwells of three minutes (180 s) each at ε_{max} and ε_{min} [21]. For better comparability, the numbering in the detail (upper right corner) follows the procedures performed in this study, which are described in more detail below.

deformation range), this practice barely reflects the actual operating conditions. So far – presumably because of the high testing effort – only a few published studies deal with creep-fatigue interactions for long dwell periods [30–34], dwell times at lowered mechanical load levels [30,33], or complex loading paths, including or using stress-controlled dwell times [30–32,35,36]. The latter should not remain unmentioned because a straightforward transferability of stress relaxation to creep processes is not always given [32,37–39].

Therefore, taking the next step towards service-like fatigue of 9–12 % Cr steels, this study extends a standard RF procedure with a low strain amplitude of $\varepsilon_a = 0.2\%$ and three-minute dwells at min/max strain (cf. Fig. 2) by including an additional 30-minute dwell period in each cycle. The load level of these additional dwells is lowered to nominally elastic deformation levels to further approach realistic conditions in flexible power plant operation. These extended, service-like (SL) tests are moreover either conducted fully strain-controlled or partially stress-controlled to evaluate the transferability of results from fatigue tests with relaxation periods and those with actual creep periods. Fractographic analyses are applied for mechanistic comparisons. Comparing the results of these dedicated experiments (with durations of approx. 900 h each) with those of our previous studies on classical dwell fatigue [21,27] performed with identical equipment and material, similarities and differences in mechanical behavior and lifetime performance are illuminated. The advantages and limitations of a fully strain-controlled and a partially stress-controlled test design are also discussed.

2. Experimental

2.1. Material and specimens

In continuation of our previous creep-fatigue studies on tempered martensite-ferritic grade P92 steel [21,27], the experiments of this study were performed on the same material batch. Its microstructure features a typical hierarchical tempered martensite-ferritic (sub-) structure with packets, blocks, and laths within former austenite grains, whose grain boundaries are decorated with $M_{23}C_6$ carbides. For further information on heat treatment, the measured chemical composition, and optical microscopy of the as-received condition, it is referred to [21]. Cylindrical specimens with a gauge diameter of 6 mm and a gauge length of 18 mm were machined from a commercial steam pipe (with a wall thickness of 48 mm) in the tangential direction, as depicted in Fig. 3. The specimen surfaces were ground ($R_z \leq 1$).

2.2. Mechanical tests and procedure

Two isothermal service-like tests were conducted in air, using a servo-hydraulic test machine with 100 kN force transducers (MTS Landmark, MTS, Eden Prairie, USA). Mechanical strains were measured by a water-cooled high-temperature extensometer (MTS-632.51F.04, MTS, Eden Prairie, USA) with an initial gauge length of 12 mm. All strain ramps of the loading paths described below in more detail were performed at a constant strain rate of 1.0×10^{-3} 1/s. Specimens were inductively heated to a target temperature of 620 °C, which was indicated and controlled by a type S thermocouple, spot-welded to the center of the gauge length to monitor temperature deviations within the gauge length. After fatigue testing, the number of cycles to failure, N_f, was determined by applying the failure criterion of 10 % load drop of the maximum peak stress against the peak stress at half lifetime.

Fig. 4a shows the temporal course of mechanical loading for the fully strain-controlled service-like relaxation (SLR) test. Starting from zero strain (point 0 in Fig. 4a), $\varepsilon_{min} = -0.2\%$ was approached (pt. 1), representing the compressive load acting on the inner wall of a thick-walled steam pipe due to hindered thermal expansion during a start-up. Since the material at the inner surface quickly reaches temperatures that allow for temperature-activated microstructural processes, it may be anticipated that parts of the (nominally elastic) compressive deformation are converted to plastic deformation. In our test procedure, this step was resembled by a three-minute dwell at constant strain (pt. 1 to pt.2). Eventually, the temperature gradients between hot inner and cool outer wall diminish, and thermal misfit stresses are reduced, which was modeled here by unloading the specimen to $\varepsilon = 0$ (pt. 2 to pt. 3). Note that the specimen may reach tensile stress here due to the previously accumulated compressive plastic deformation. In the subsequent 30-minute dwell time in strain control at $\varepsilon = 0$ (pt. 3 to pt. 4) that was intended to emulate a phase of steady-state operation (SSO), this tensile stress was allowed to relax. Within the subsequent steps (pt. 4 to pt. 6), a shutdown-like phase followed, which simulated ventilation of the hot pipe with a colder medium, leading to contraction and, thus, tensile loads at the pipe's inner surface. Accordingly, the test procedure comprised approaching the maximum tensile strain ($\varepsilon_{max} = 0.2\%$) and keeping it constant for another three minutes. Finally, the cycle was closed by a ramp to zero strain (pt. 7).

Alternatively, a partly stress-controlled service-like creep test (SLC) was performed, as illustrated in Fig. 4b: Cyclic loading, including the three-minute dwells at minimum/maximum strain, was performed analogously to the SLR test. However, in contrast to the SLR test, the 30-minute SSO was stress-controlled to impose real creep deformation on the specimen during steady-state operation. On reaching $\varepsilon = 0$ (pt. 3), strain control was, hence, switched to force control, and the stress (force) value reached at zero strain was kept constant for 30 min (until pt. 4). From the strain value present at point 4, the cycle was finished in

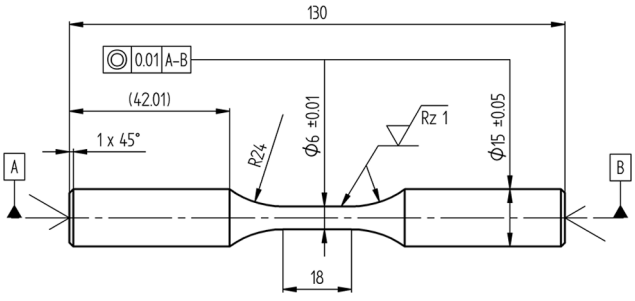

Fig. 3. Specimen dimensions (unit: mm) from [21] by Jürgens et al., licensed under CC BY 4.0.

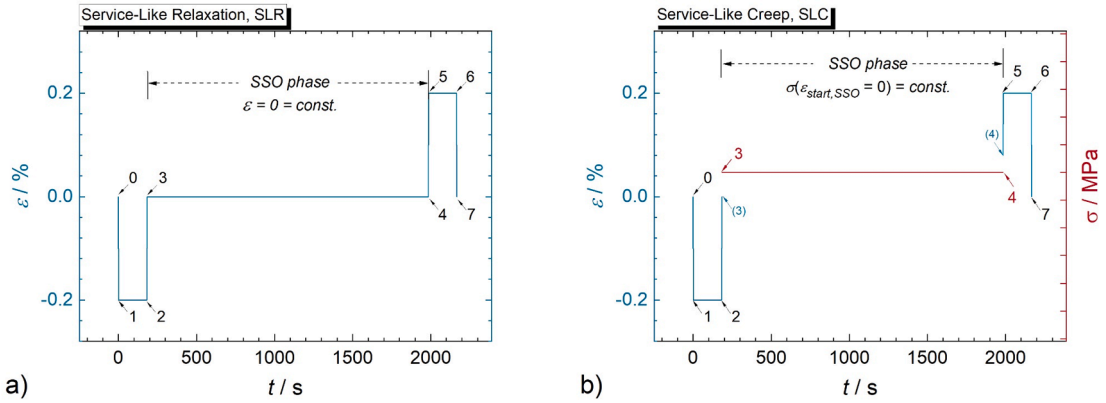

Fig. 4. Loading paths of service-like (SL) tests with three-minute dwells at minimum and maximum strain and 30-min steady-state operation (SSO) phases in between for (a) service-like relaxation (SLR) test with SSO at $\varepsilon = 0$; (b) service-like creep (SLC) test with SSO at stress values obtained at zero crossing of strain in each cycle.

strain control. It is finally noted that both SL tests are variations of the standard RF test procedure, illustrated in Fig. 2. They differ from the latter by an opposite loading direction at the beginning of the test (i.e., initial compressive loading in SL tests versus tensile loading in the RF test) and the additional SSO periods at lowered load levels described above.

It is acknowledged that the proposed SLR and SLC model cycles cannot fully mimic the operation condition of any actual power plant component since all parameters were chosen arbitrarily. Furthermore, important additional contributions, such as the varying operational pressure and the resulting complex stress states, are not considered. Nevertheless, this is a reasonable and justifiable simplification and allows to demonstrate the basic material's reaction to different combinations of cyclic and monotonous loading phases.

2.3. Fractographic analyses

After failure, the fracture surfaces of both specimens as well as longitudinal sections of fractured specimen halves were analyzed in bright-field optical microscopy. Preparation of the longitudinal sections included i) cutting the specimen halves longitudinally using a low-speed laboratory wet cutting machine, ii) embedding the fragments in cold-curing epoxy resin, iii) semi-automatic metallographic grinding on SiC abrasive paper down to a grit size of 1200, and iv) polishing to 1 μm using diamond suspension.

3. Results and discussion

Fig. 5 shows the temporal courses of stress and strain in four selected cycles for SLR (Fig. 5a) and SLC (Fig. 5b). It visualizes time-dependent inelastic deformations in all constant load periods (dwell times, DTs) and illustrates some related basic definitions. During each strain-controlled DT – i.e., the first, the intermediate (SSO), and the last DT in each SLR cycle and the first and the last DT in each SLC cycle – the mechanical stress relaxes as a function of the start stress level (σ_{start}) and DT duration by an amount σ_r. This stress relaxation, σ_r, corresponds to the difference between the initial (σ_{start}) and final stress values (σ_{stop}) within a single DT. In each stress-controlled DT – i.e., in the intermediate DT (SSO) in each SLC cycle, a creep strain ($\varepsilon_{c,SSO}$) develops, which is obtained from the difference between the final (ε_{stop}), and initial value of strain (ε_{start}), cf. Fig. 5b.

Alternatively, the corresponding stress–strain hystereses of the SLR and SLC tests are depicted in Fig. 6a/b, for the initial cycle and at half of the lifetime (0.5 N_f). The results of a corresponding RF test with $\varepsilon_a = 0.2$ % (cf. Fig. 2) and of a continuous LCF test from earlier work are included for direct comparison. Naturally, this type of plot cannot display the evolution of stress and/or strain as a function of time during the

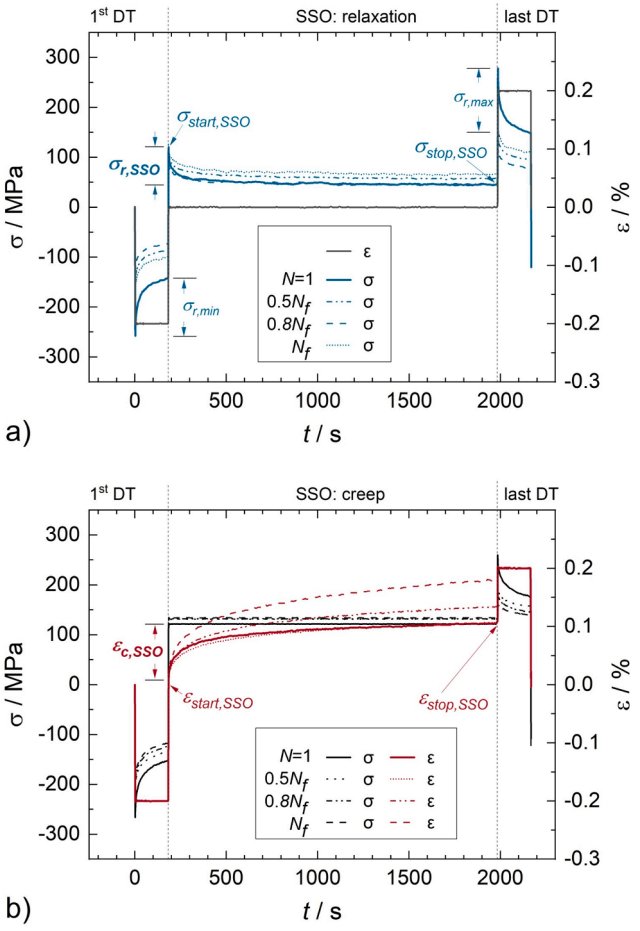

Fig. 5. Temporal courses of stress and strain within selected individual cycles for (a) SLR and (b) SLC. Illustrated σ- and ε-definitions refer to values of the respective first cycles and may serve as graphical complements to the descriptions within the text part. Relative times (t) on abscissae of these plots refer to individual cycles. Stress curves in (b) are almost identical for the SSO periods of different cycles and, hence, appear superimposed.

different DTs. However, these diagrams allow to comprehend more easily how the DTs affect the further course of the load paths.

As each SLR and SLC cycle contains 36 dwell minutes at high temperature in total, it is not surprising that pronounced creep-fatigue interactions in both SL tests alter the global cyclic softening behavior and reduce the fatigue life (N_f) compared to the corresponding standard LCF

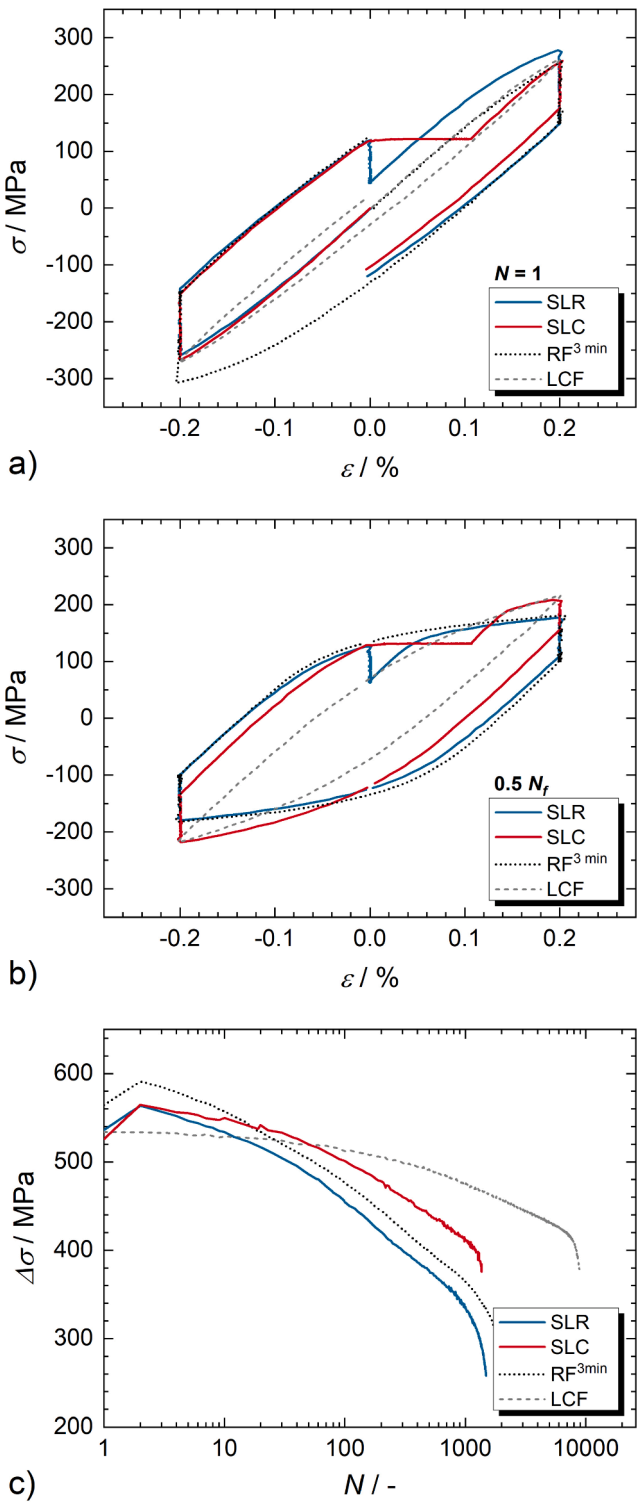

Fig. 6. Stress–strain hystereses of the SLR and SLC test in (a) the first cycle, and (b) at 0.5 N_f. The corresponding hystereses of a previous RF test (cf. Fig. 2) and a LCF test, both performed on the same material batch in a previous study [21], are included for comparison purposes. (c) Cyclic deformation curves showing the evolutions of $\Delta\sigma$ in the SLR, SLC, RF and LCF tests with $\varepsilon_a = 0.2$ %.

(no dwells, [21]) and RF tests (e.g., six minutes per cycle, [21]). Fig. 6c, giving the stress response over the number of cycles for the SL and various standard tests performed at $\varepsilon_a = 0.2$ %, readily evidences these anticipations. In addition, Fig. 5 and Fig. 6 indicate that fundamentally different stress and strain evolutions within individual SSOs for SLR and SLC affect the mechanical behavior in subsequent transient load shifts and DTs. Consequently, apparent deviations in the global deformation behavior between SLR and SLC emerge that enlarge with the number of cycles. To decompose these complex interactions, long-term stress relaxation and creep strain evolution in the SSOs will be discussed first (Section 3.1). Afterward, their impact on the global deformation behavior will be illuminated (Section 3.2). Based on the subsequent mechanistic analysis and interpretation (Section 3.3), the advantages and disadvantages of different experimental designs will be evaluated (Section 3.4).

3.1. Creep deformation in long-term stress- and strain-controlled SSOs at low mechanical load

The time- and load-dependent transformation of elastic into inelastic creep strain during quasi-static loading periods may, in principle, be determined via Eqs. (1) and (2) since the total strain (ε_t) is generally composed of the spontaneously occurring, time-independent load strain ($\varepsilon_0 = \varepsilon_{start}$) with elastic ($\varepsilon_{el}$) and possibly initial plastic components ($\varepsilon_{pl,i}$) and the time-dependent creep strain (ε_c). For the case of the SSO periods in this study, the plastic term in Eqs. (1) and (2) can be omitted since the mechanical loads were so low that the acting stresses of approx. 120 MPa to 135 MPa (cf. Fig. 5) are safely below the cyclic yield point of the material ($\Delta\sigma_{cyc}/2 = 238$MPa at 620 °C from [27]).

$$\varepsilon_t = \varepsilon_o + \varepsilon_c = \varepsilon_{el} + \varepsilon_{pl,i} + \varepsilon_c \tag{1}$$

$$\varepsilon_c = \varepsilon_t - \varepsilon_{el} - \varepsilon_{pl,i} \tag{2}$$

Therefore, for the stress-controlled SSO in the SLC test, the creep strain at any time, $\varepsilon_{c,SSO(SLC)}(t)$ can be calculated with Eq. (3) from the difference between the momentary total strain, $\varepsilon_t(t)$, and the initial elastic strain ($\varepsilon_{el} = \varepsilon_{start,SSO}$), which is zero in this particular case.

$$\varepsilon_{c,SSO(SLC)}(t) = \varepsilon_t(t) - \varepsilon_{start,SSO} = \varepsilon_t(t) - 0 \tag{3}$$

Accordingly, the creep strain generated during a complete SSO, $\varepsilon_{c,SSO(SLC)}$ is equal to the measured total strain at the end of the SSO ($\varepsilon_t = \varepsilon_{stop,SSO}$) (Eq.4). In other words, since the SSO starts at $\varepsilon_t = \varepsilon_{start,SSO} = 0$, the total strain measured during the SSO is creep strain.

$$\varepsilon_{c,SSO(SLC)} = \varepsilon_{stop,SSO} - \varepsilon_{start,SSO} = \varepsilon_{stop,SSO} - 0 = \varepsilon_{stop,SSO} \tag{4}$$

For the SSO in the SLR test, the time-dependent creep strain is not directly measurable but can be calculated for each time increment using Eq. (5): A purely elastic initial load with stresses below the yield point is also hypothesized, and the time-dependent strain is thus directly related to the elastic strain component via the time-decreasing remaining stress $[\sigma_{start,SSO} - \sigma(t)]$ according to Hooke's law [30].

$$\varepsilon_{c,SSO(SLR)}(t) = \frac{\sigma_{start,SSO} - \sigma(t)}{E} \tag{5}$$

Consequently, for the entire duration of the SSO, Eq. (6) can be used to determine a final creep strain value for an individual SSO in the SLR test.

$$\varepsilon_{c,SSO(SLR)} = \frac{\sigma_{start,SSO} - \sigma_{stop,SSO}}{E} \tag{6}$$

In our study, Young's modulus (E) was set to 151 GPa, as determined for $T = 620^{\circ}$C in [27], and was treated as invariant over the entire fatigue life.

Fig. 7 presents the temporal evolution of the creep strain, $\varepsilon_{c,SSO}(t)$ during individual SSOs in the SLR (blue curves; Eq. (5)) and SLC test (red; Eq. (3)) exemplarily for $N = 1$, $0.5N_f$, and N_f. Fig. 7a readily reveals that the magnitudes of creep deformation for stress relaxation and true creep are only comparable in a very narrow time frame of approx. one second within the primary creep stage. The reason for this lies in the pronounced stress dependence of the creep strain and creep strain rate for transient and viscous creep processes, especially for dislocation creep

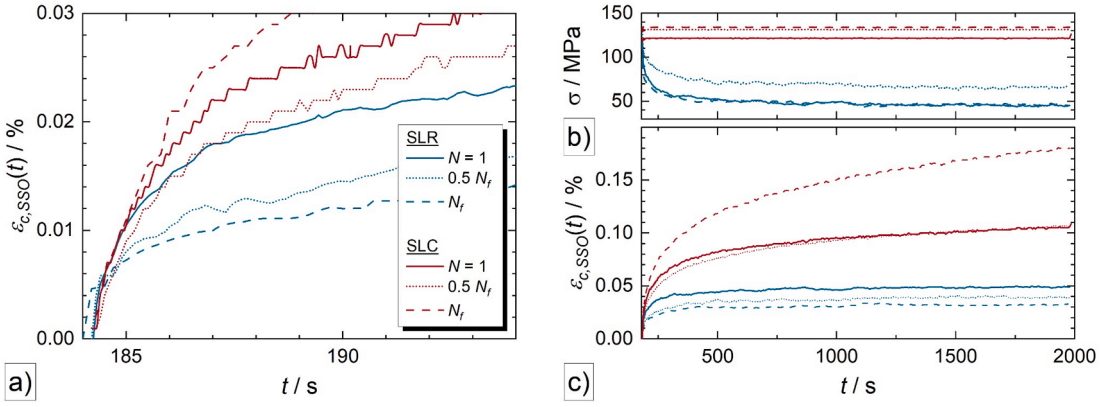

Fig. 7. Creep strain evolution (cf. Eq. (3) and (5)) during the SSO periods for the first, the half-life, and N_f cycles in SLR and SLC tests: (a) ε_c evolution within the first seconds of the SSOs (discontinuities originate from signal noise at high magnification); (b) σ scaled for total (30-min) SSO durations, and (c) ε_c scaled for total SSO durations.

[40]: While σ remains constantly high during the SSOs in the SLC test (red; Fig. 7b), it decreases continuously in the SLR test (blue; Fig. 7b), such that the creep processes slow down quickly after the rapid stress drop at the beginning of the SSO in the SLR test (Fig. 7b,c). In fact, from about 500 s onwards, the creep strain tends to saturate in the SLR test (Fig. 7c), and $\varepsilon_{c,SSO(SLR)}(t)$ appears almost constant for $t > 500$s.

Fig. 7 also demonstrates that $\varepsilon_{c,SSO}$ is not only a function of the dwell type but also of the number of cycles. This becomes even clearer in Fig. 8, where the start ($\sigma_{start,SSO}$, $\varepsilon_{start,SSO}$) and stop ($\sigma_{stop,SSO}$, $\varepsilon_{stop,SSO}$) values of stress and strain, $\sigma_{r,SSO}$ and $\varepsilon_{c,SSO}$, are presented exemplarily for those cycles listed in Table 1. Due to the rapid stress decay during individual SSOs in the SLR test and the diverging creep strain evolution for SLR and SLC (Fig. 7), it is consistent that $\varepsilon_{c,SSO(SLR)}$ is generally significantly lower (at least 50 %, depending on N) than $\varepsilon_{c,SSO(SLC)}$ in Fig. 8a.

Interestingly, $\varepsilon_{c,SSO}$ decreases within the first approx. 100 cycles markedly for SLC (Fig. 8a; semi-filled red diamonds) and less pronounced also for SLR (Fig. 8a; blue semi-filled squares) despite rising σ_{start} values for SLR in this cycle range (Fig. 8b; blue squares). That means the strain hardening typical for the primary creep region [40] seems to outweigh competing softening processes in this cycle region, which cannot directly be discerned in the global softening behavior of both complex SL tests (Fig. 6). The fact that the start stresses increase here at all is related to the necessary re-deformation of the specimens up to $\varepsilon = 0$, which were plastically deformed in compression (point 0 to point 1 in Fig. 4) before the SSO and consequently irreversibly compressed in the first cycles. These kinematic hardening effects are explained in Section 3.2 in more detail.

Once the "primary creep" region is overcome, the creep strains per SSO grow steadily in the SLC test (Fig. 8a; semi-filled red diamonds), whereby the slight increase of the start stress level (filled red diamonds in Fig. 8b) may accelerate the creep processes additionally, especially in the second half of the fatigue life. Fundamentally different from this, an increase in $\varepsilon_{c,SSO}$ does not occur with the strain-controlled SSOs in the SLR test (semi-filled blue squares in Fig. 8a). Moreover, in the second half of the SLR fatigue life, the $\varepsilon_{c,SSO(SLR)}$ evolution within individual SSOs appears to remain nearly independent of cycle number over a wide cycle range, although $\sigma_{start,SSO(SLR)}$ decreases here markedly with the

Table 1
Selected cycles for stress- and strain values shown in Fig. 8 and Fig. 9.

N(RF)	N(SLR)	N(SLC)	Remarks
1	1	1	–
2	2	2	–
3	3	3	–
4	4	4	–
5	5	5	–
10	10	10	–
20	20	20	–
50	50	50	–
100	100	100	–
200	150	140	$\approx 0.1N_f$
510	370	340	$\approx 0.25N_f$
1030	740	690	$\approx 0.5N_f$
1640	1180	1100	$\approx 0.8N_f$
1840	1330	1230	$\approx 0.9N_f$
2040	1470	1360	$N_f - 10$

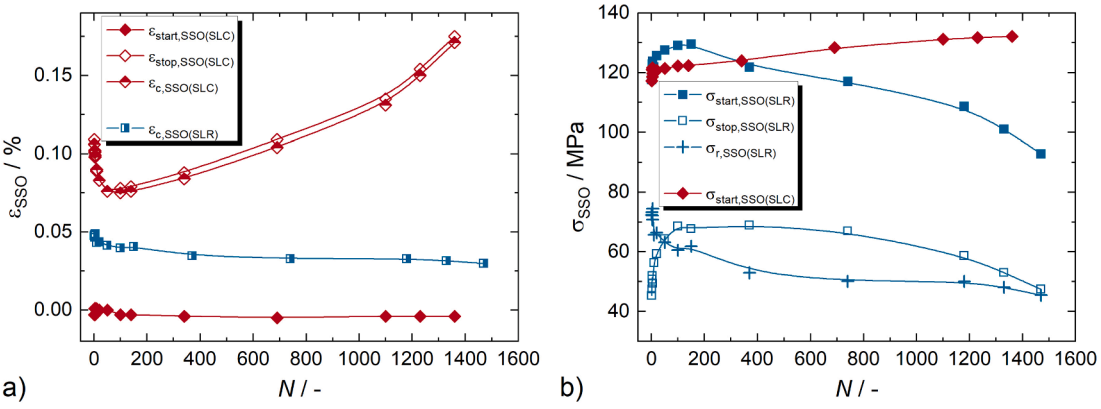

Fig. 8. Strain and stress values for selected SSO periods of various cycles (as listed in Table 1): (a) $\varepsilon_{c,SSO(SLC)}$ determined from $\varepsilon_{stop,SSO}$ and $\varepsilon_{start,SSO}$ (Eq. (4)) vs $\varepsilon_{c,SSO(SLR)}$ (Eq. (6)); (b) corresponding start- ($\sigma_{start,SSO}$), stop- ($\sigma_{stop,SSO}$), and relaxation stress ($\sigma_{r,SSO}$), values.

number of cycles (Fig. 8b; full blue squares). This observation indicates that the relaxation processes during the SSOs in the late fatigue stage, where the start stress levels are very low, may rather be determined by the SSO duration (i.e., time) than by stresses or strains alone, and a continuous change of creep mechanisms may therefore be anticipated.

3.2. Impact of long-term stress- and strain-controlled SSOs at low mechanical load on the global creep-fatigue behavior

The experimental design presented in this study does not serve the sole purpose of comparing extended relaxation and creep dwell times but is specifically intended to shed light on their divergent effects on subsequent load changes and the global material behavior in complex loading conditions. For this reason, the start stress (σ_{start}) values of the three-minute, strain-controlled (first and last) DTs at ε_{max} or ε_{min}, which are identical to the peak stress values (σ_{max} or σ_{min}) of each cycle, are plotted versus the number of cycles, N for the SLR, SLC and RF tests in Fig. 9. These and the corresponding values of σ_{stop} and σ_r were determined exemplarily for the same cycles selected for the SSOs (cf. Table 1). The subfigures are arranged according to their logical order of appearance within the loading sequence, i.e., Fig. 9a,c on the left side correspond to the 1st DTs and Fig. 9b,d on the right to the last DTs in each cycle. The plots include the characteristic points of DTs in tension and compression. All compressive stresses were inverted to positive values in these diagrams to allow direct comparisons of the evolutions from both loading directions. This approach was followed since the investigated material exhibited a pronounced initial tension/compression symmetry as well as nearly similar softening behavior in tension and compression during continuous LCF tests in our previous investigations [21].

The global cyclic softening from $N = 2$ of RF, SLR, and SLC shown in Fig. 6 (for $\Delta\sigma$) is also reflected in the σ_{start} curves for the first and last DTs of each cycle (Fig. 9a,b; full symbols), in which the peak strains were kept constant for three minutes each. However, $\sigma_{start,1stDT}$ (Fig. 9a) and $\sigma_{start,lastDT}$ (Fig. 9b) are asymmetric with respect to the absolute values (e.g., $\sigma_{start,1stDT} > \sigma_{start,lastDT}$ for SLR and SLC). This means that the peak stress response seems strongly dependent on the loading history when DTs are implemented. The stress relaxations, σ_r in the first and last DTs, performed at higher constant strains than in the SSOs, depend on the start stress level for all types of tests shown. Consequently, similar asymmetries between the first and last DTs are also observed in σ_{stop} (open squares in Fig. 9a,b) and σ_r (Fig. 9c,d). Moreover, the σ_r curves hardly vary in the first DTs despite different test designs (Fig. 9c) but strongly deviate in the last DTs (Fig. 9d). The SSOs, with their different dwell conditions and their resulting deformation processes, have apparently a strong impact on the behavior in the directly following last DT. These effects, as well as the initial strain hardening occurring between the first and the second cycle, can be partly explained by the re-deformation effects related to kinematic hardening frequently observed, e.g., in [21,28,30,41] and described in the following in more detail:

For all types of tests discussed, a time-independent elastic–plastic deformation ($\varepsilon_0 = \varepsilon_{el} + \varepsilon_{pl,i}$) occurs at the beginning of the test ($N = 1$) between points 0 and 1 of mechanical loading (cf. Fig. 2 and Fig. 4), which is already associated with an irreversible change in shape (i.e., $\varepsilon_{pl,i}$). During the subsequent strain-controlled first DT, up to point 2, some of ε_{el} is converted into $\varepsilon_{c,1stDT}$ so that ε_{el} decreases until the end of the DT, and the specimen gets partly unloaded (σ relaxes) despite a constant total strain during the DT. The simultaneously increasing creep strain adds to the initial plastic strain and raises the inelastic (irreversible) strain component, ε_{in} ($\varepsilon_{in} = \varepsilon_{pl,i} + \varepsilon_c$). Therefore, a stress-free state ($\sigma = 0$, $\varepsilon_{el} = 0$) is reached already shortly after point 2 during the

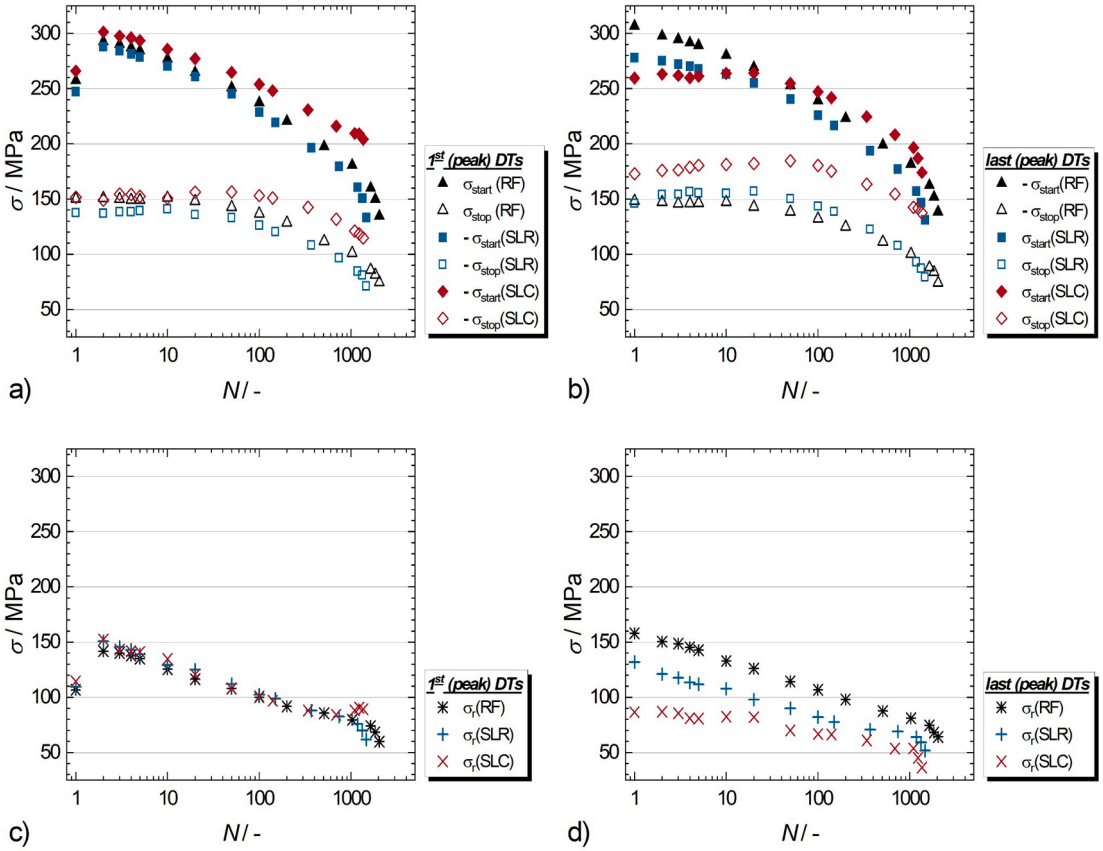

Fig. 9. SLR, SLC, and RF stresses in three-minute DTs at ε_{max} and ε_{min} (i.e., stresses in the first and last DTs) arranged according to their chronological appearance in the respective loading path (cf. Fig. 2 and Fig. 4): (a, b) start and stop stresses for the first and last DT in each selected cycle, respectively; (c, d) corresponding stress relaxations. All compressive stresses are inverted (to positive values) for the sake of comparability. RF data taken from a previous study [21].

subsequent ramp between points 2 and 3 though the specimen is still irreversibly compressed in the SL tests (strained in the RF test). To reach a target strain value of, e.g., $\varepsilon_t = 0$ (pt. 3), an effectively higher irreversible strain increment (with the magnitude of ε_{in}) than in a test without DTs must thus be overcome upon load reversal during this second ramp. Hence, higher stresses than in a classical LCF test are generated during load reversal in tests with strain-controlled dwells.

In the case of the RF test, this target strain value after the first load reversal corresponds to $\varepsilon_{t,min} = -0.2\%$ (cf. point 5 in Fig. 2), where σ_{start} of the last (second) DT in the first cycle (Fig. 9b; full black triangles) is noticeably increased compared to that in the first DT (Fig. 9a). Such re-deformation effects will still occur after elastic–plastic deformation at each load reversal in the following cycles. However, they will weaken from cycle to cycle as i) high proportions of the cyclic deformation are microscopically linked to slip reversibility, ii) the peak strains are confined to a constant value (±0.2 %) by the experimental design, and iii) the continuous stress reduction by relaxation processes in previous DTs and cycles lowers the driving force for the conversion of ε_{el} to ε_c during the three-minute DTs. In other words, σ_{start} and σ_{stop} decrease from then on (Fig. 9 a, b) because less creep strain is produced per three-minute strain-controlled DT as the number of cycles increases, and the strain to be effectively supplied ($= \varepsilon_{in}$) at each load reversal must consequently decrease successively with from the second cycle onward.

The cyclic deformation behavior of the SL tests in the last DTs within the first cycles (Fig. 9b) and the deviations from the RF test can also be explained by such reverse deformation effects. As mentioned earlier, the inelastic strain must be overcome during load reversal, thus subjecting the specimens in both SL tests under elastic tensile stress at $\varepsilon_t = 0$ (point 3 in Fig. 4). For the SLR test, part of this elastic tensile stress, $\sigma_{start,SSO(SLR)}$ is now reduced by relaxation processes (competing creep and recovery) during the 30-minute SSO at $\varepsilon_t = 0$. The subsequent ramp toward $\varepsilon_{t,max}$ (points 4 to 5) in the SLR test hence causes lower $\sigma_{start,lastDT}$ (Fig. 9b; full blue squares) and thus lower stress relaxations (Fig. 9d) than in the RF test, where this additional time-dependent reduction of elastic strain and stress at $\varepsilon_t = 0$ is not possible due to the absent SSO.

In the SLC test, in contrast, no macroscopic stress relief occurs during the SSO. Instead, the stress is kept constant, and a creep strain, $\varepsilon_{c,SSO(SLC)}$, develops, whereby the specimen is free to elongate without geometric constraint. At the end of the SSO in the first cycle (point 4 in Fig. 4b), the specimen is already strained by approx. 0.1 % while the stress remains constant. Consequently, between points 4 and 5, only about 0.1 % additional strain ($\varepsilon_{t,max} - \varepsilon_{stop,SSO(SLC)}$) needs to be effectively applied to reach the target value of $\varepsilon_{t,max} = 0.2\%$ in the SLC test whereas 0.2 % (with $\varepsilon_{stop,SSO(SLR)} = 0$) are required in the SLR test. The reduced necessary loading increment ($\varepsilon_{t,max} - \varepsilon_{stop,SSO(SLC)}$) during the ramp between points 4 and 5 is responsible for the lowest $\sigma_{start,lastDT}$ values in SLC in the early fatigue stage (Fig. 9b; full red diamonds). These and the lowered driving force for stress relaxation and the conversion of elastic strain into creep strain during the last DTs lead to throughout higher $\sigma_{stop,lastDT}$ (Fig. 9b; open red diamonds) and the lowest $\sigma_{r,lastDT}$ values (Fig. 9d; red symbols).

3.3. Mechanistic analysis

As shown in Section 3.1, the mechanical behavior differs for both SL tests. Although an in-depth microstructure elucidation is not the aim of this study, an attempt is made in the following to interpret the mechanical behavior based on established knowledge of creep mechanisms and microstructure evolution during creep, relaxation, and fatigue to derive the advantages and disadvantages of both test designs.

The microstructural matrix or grain boundary damage that occurs during classical creep tests under tensile loads depends largely on the load- and temperature-specific prevailing creep mechanisms (dislocation glide, dislocation climb (power-law creep), and diffusional flow) [40]. Although the widely used deformation mechanism maps by, e.g., Frost and Ashby [42], are not available for each specific steel (and microstructure) and do not account for transient load shifts due to creep-fatigue. Though neglecting kinematic hardening effects, they, nevertheless, allow a rough approximation of the expected idealized steady-state creep mechanisms for the 30-minute SSOs examined in this study. The deformation mechanism maps shown in Fig. 10 were constructed for a highly alloyed fcc 304 steel with a grain size of 50 µm [42], for a low-alloy 1 %CrMoV bcc steel with a grain size of 100 µm [42], and a bcc P91 steel [43] belonging to the group of 9–12 %Cr steels investigated in this study. For the sake of comparability, all data were plotted in the form of normalized equivalent shear stress (σ_s/G) vs homologous temperature T/T_m. Herein, the equivalent shear stress according to [42] is $\sigma_s = \sigma/\sqrt{3}$, the shear modulus is $G \approx E/[2 \times (1+\nu)]$ with ν being Poisson's coefficient, and T_m refers to the melting temperature.

Following this conversion and using $E = 151$GPa and $\nu = 0.3$, σ_s/G values were calculated for different time steps within individual SSOs of four selected cycles for both test types, as listed in Table 2. The σ_s/G values plotted in Fig. 10 correspond to $t_{SSO} = t_2 \approx 500$s, which may represent times in the transition region from primary to secondary creep within the SSOs or times after a rapid initial stress relaxation in the SLR test, alternatively. Due to numerical similarities of the calculated σ_s/G values, some symbols in Fig. 10 appear almost superimposed for different cycles of the same test type. However, this rough approximation is helpful in that it suggests different prevailing creep mechanisms for stress-controlled SSOs in SLC (red open diamonds in Fig. 10) and strain-controlled SSOs in SLR (open blue squares).

For the SLC test, dislocation creep is expected to be the rate-determining creep mechanism, whereas rate-determining should, however, not be confused with being the exclusive creep mechanism. In fact, dislocation climb and diffusional flow (and recovery) almost always superimpose. The associated processes such as the dislocation multiplication by creep plasticity and crystal recovery (annihilation and rearrangement to possibly coarsening low-energy subgrain boundaries [44]) compete, possibly causing a quasi-stationary equilibrium state between hardening and softening in the secondary creep stage. It is important to understand that primary and secondary (dislocation) creep thus do not necessarily reduce the global dislocation density and, unlike relaxation, do often not contribute significantly to a global release of elastic lattice distortion (residual stresses) [45,46].

Due to the usually developing cellular dislocation networks and

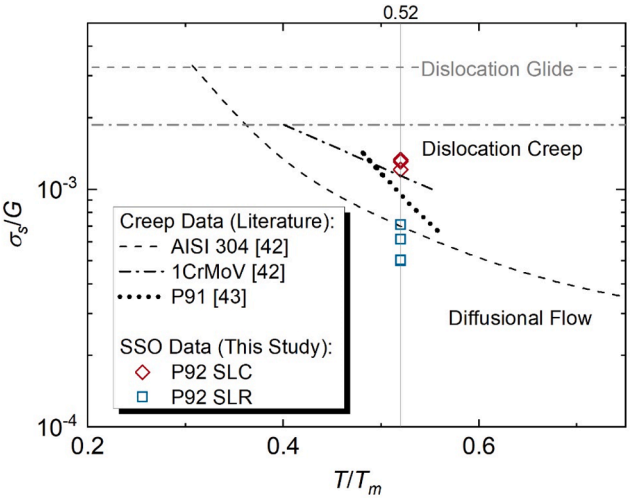

Fig. 10. Creep deformation mechanism maps of three different steels adapted from curves and data in [42,43], showing idealized transitions from dislocation glide to dislocation creep (grey lines) and from dislocation creep to diffusional flow (black lines). Creep and relaxation data for SSOs of four SLC- and SLR cycles from this study (P92) refer to σ_s/G values at $t_2 \approx 500$s (grey column in Table 2) and $T/T_m \approx 893\text{K}/1723\text{K} = 0.52$.

Table 2
Normalized shear stress σ_S/G (SSO) input data for deformation mechanism analysis of SLC and SLR in Fig. 10, as calculated from stress values at different relative times ($t_1 = 0s; t_2 \approx 500s; t_3 \approx 1795s$) in individual SSOs. For a more detailed description, the reader is referred to the text. Approximated normal ($\dot{\varepsilon}$) and shear strain rates ($\dot{\gamma} = \sqrt{3}\dot{\varepsilon}$) are also provided for potential future analyses of P92.

	N	σ_{SSO}/MPa			σ_S/MPa			σ_S/G			$\dot{\varepsilon}$		$\dot{\gamma}$	
		t_1	t_2	t_3	t_1	t_2	t_3	t_1	t_2	t_3	$t_2 - t_1$	$t_3 - t_2$	$t_2 - t_1$	$t_3 - t_2$
SLC	1	119	122	122	69	70	70	1.2E−03	1.2E−03	1.2E−03	1.8E−06	1.4E−05	3.0E−06	2.4E−05
	690	129	131	131	75	76	76	1.3E−03	1.3E−03	1.3E−03	1.7E−06	1.7E−05	2.9E−06	2.9E−05
	1100	131	132	132	76	76	76	1.3E−03	1.3E−03	1.3E−03	2.1E−06	2.4E−05	3.6E−06	4.1E−05
	1370	131	134	134	76	77	77	1.3E−03	1.4E−03	1.4E−03	2.7E−06	3.6E−05	4.6E−06	6.3E−05
SLR	1	120	51	45	69	29	26	1.2E−03	5.1E−04	4.5E−04	9.2E−07	3.0E−08	1.6E−06	5.2E−08
	740	127	71	67	73	41	38	1.3E−03	7.2E−04	6.7E−04	7.3E−07	2.3E−08	1.3E−06	4.1E−08
	1180	117	62	58	67	36	33	1.2E−03	6.2E−04	5.8E−04	7.3E−07	2.2E−08	1.3E−06	3.8E−08
	1480	96	50	45	55	29	26	9.6E−04	5.1E−04	4.6E−04	6.0E−07	2.6E−08	1.0E−06	4.4E−08

subgrain boundaries, sharp deformation gradients may form within individual crystallites over time, which, together with pile-up effects at grain boundaries (and precipitates) and with the voids constantly developing during the climbing of edge dislocations, lead to the nucleation and coalescence of creep pores in the tertiary region of creep at the latest [40]. The typical appearance of such creep damage, with pore nucleation in the bulk and subsequent crack formation at/propagation along these pores, can be assumed for the SLC specimen, cf. the polished longitudinal section in Fig. 11a. The micrograph clearly exhibits pore formation, with increasing intensity towards the final fracture on the left of the image, and a serrated crack path. Since i) pore formation and coalescence are not observed to the same extent in the SLR test (cf. Fig. 11b) and ii) $\varepsilon_{c,SSO(SLC)}$ increases significantly with the number of cycles, i.e., the creep processes accelerate increasingly with N (Fig. 8a), the creep damage generated during the SSOs in the SLC test likely becomes dominant for the overall damage in the advanced fatigue stage at the latest.

These assumptions seem only partially valid for the relaxation processes during the SSOs in the SLR test since the acting (shear) stresses, in contrast to the SLC test, do not remain constant over time but decrease during each SSO. For example, for $t_{SSO} \geq 500s$, a shift from dislocation creep towards "diffusional flow" is suggested in Fig. 10 by σ_s/G (blue squares) lying below the black reference transition lines. Hence dislocation annihilation (recovery) could become more relevant than in the SLC test. Consequently, in contrast to SLC, elastic lattice distortion could actually be relieved during relaxation dwells, provided the stress level is sufficiently low and DT duration sufficiently long, as observed in [45,46] and demonstrated in this study. Against this background, a faster softening in the SLR than in the SLC test (Fig. 6) seems plausible.

The longitudinal section of the SLR test piece (Fig. 11b) provides no evidence of more severe grain boundary damage associated with early pore formation at the grain boundaries due to vacancy diffusion under diffusional creep: The apparent porosity seems to be lower than in the SLC test, and both the fracture edge and individual transverse cracks

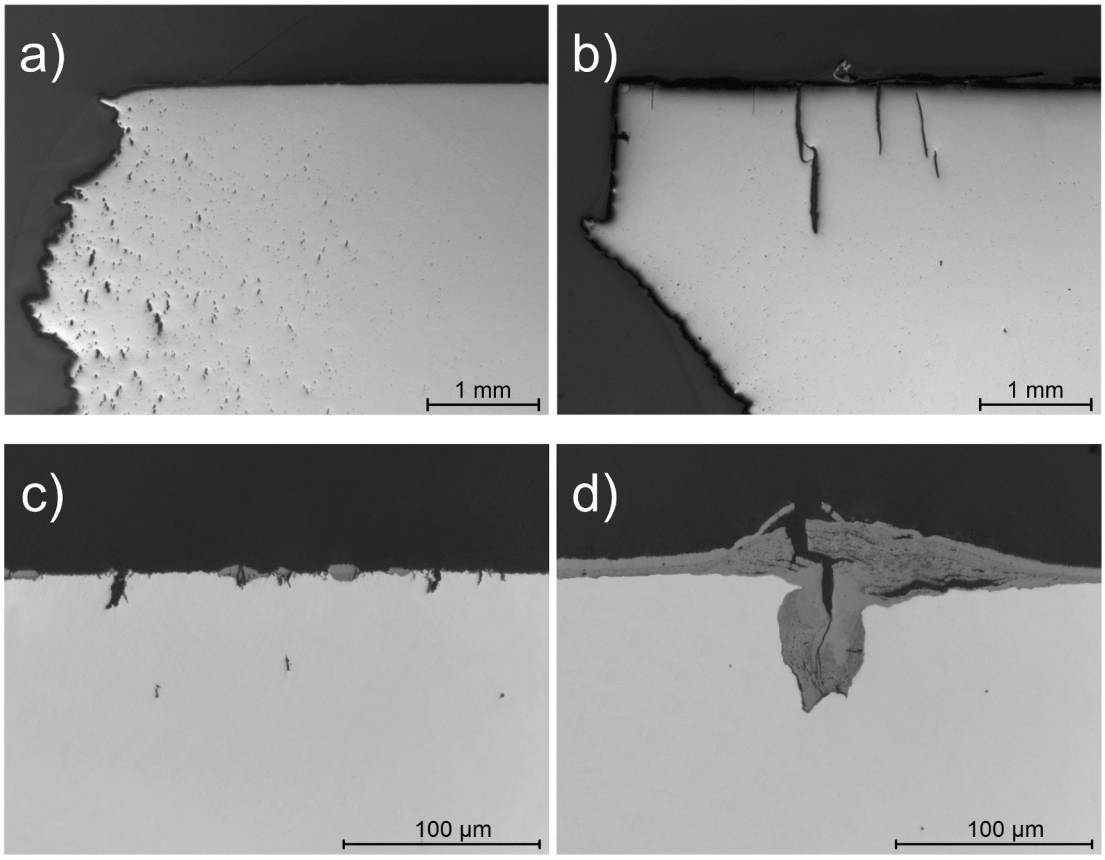

Fig. 11. Longitudinal sections of fractured SLC- (a, c) and SLR specimen (b, d) (optical bright-field microscopy).

originating from the specimen surface are remarkably straight, suggesting transgranular crack propagation. As the deformation maps in Fig. 10 are highly simplified models, e.g., focusing on creep and not considering static or dynamic recovery processes separately, this observation does not contradict the hypothesis of different microstructural damage mechanisms for SLR and SLC. In fact, the fracture surface in Fig. 12b reveals typical high-temperature fatigue damage with multiple incipient cracks on the specimen surface. That means an apparently higher number of (micro- and) macrocracks than observable on the ductile fissured SLC fracture surface (Fig. 12a) certainly contributes to an accelerated macroscopic softening in SLR.

Furthermore, Fig. 11d reveals another important mechanistic difference in the SLR test compared to the SLC test (Fig. 11c): Since cracks nucleate in the former more frequently at the lateral surface while being constantly in contact with oxygen, and cracks are opened in tension at the beginning of each 30-minute SSOs and also in the three-minute DTs at ε_{max}, local oxidation processes at surface cracks are facilitated. These local oxidations, in turn, presumably accelerate macrocrack initiation and growth, which could also enhance macroscopic softening. Since only comparatively thin oxidation layers form in the SLC test, as was similarly observed in [31], but extraordinarily multilayered and thick oxide layers emerge in the SLR test despite identical DT durations and test temperature, a strong mutual influence of crack propagation and local oxidation in the SLR test must be assumed. It is, however, acknowledged that further testing under different loading conditions would be required to clarify the importance of surface crack nucleation and oxidation in comparison to creep-based cavity nucleation in the bulk. In this respect, the impact of multiaxiality (often associated with hydrostatic stress components) on these damage processes requires to be clarified to enable a successful transformation of results to the technical application.

3.4. Advantages and disadvantages of SLR and SLC testing procedures

The standard procedure of implementing strain-controlled dwell times at min/max strain into LCF cycles to study creep-fatigue interactions presumes that stress relaxation and creep processes are sufficiently comparable in the parameter space studied. And indeed, based on a mere fatigue life comparison of the two types of tests (similar N_f in Fig. 13), one could conclude that this transferability is also given for the tests with additional stress- and strain-controlled dwells investigated in this study.

However, the detailed mechanical analysis of different deformation phases in individual cycles and their mutual influence, the macroscopic cyclic softening behavior, and the microscopic damage in fracture surfaces and longitudinal sections draw a different picture:

For long dwell times and low stresses (SSOs), grain boundary damage (due to diffusional creep) presumably superimposes with higher

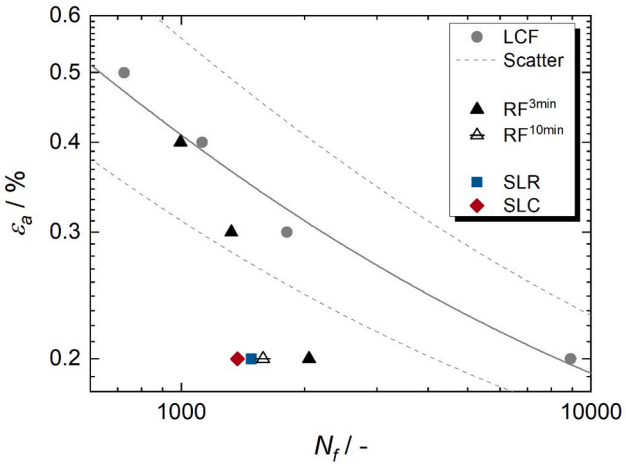

Fig. 13. Comparison of fatigue life in standard LCF tests [21], RF tests with symmetrical three- and ten-minute DTs [21], and the service-like tests performed in this study.

viscoplastic deformations (dislocation glide and climb) in stress-controlled dwell times, while recovery (diffusional creep, dislocation climb) and, after fatigue-induced crack initiation at the surface, also oxidation seem to be the dominant damage mechanisms in long strain-controlled dwells at low mechanical loads. These mechanistic differences during SSO periods cause different deformation states at the end of the respective SSOs, which in turn govern the (kinematic) hardening and softening capacities during subsequent load shifts and relaxation periods (DTs at max/min strain). The fact that similar lifetimes are achieved for both exemplified test types despite these obviously different damage mechanisms can hardly be explained by referring to the surprisingly rare literature (for 9–12 %Cr steels or other high-temperature material groups) dealing with comparative fractography and microstructure investigations for long-term relaxation and creep.

The limited experimental findings presented here may only be considered as a preliminary screening for possible material reactions to combined loading scenarios. Due to the current lack of a sound mechanistic understanding of microstructural creep- and relaxation-fatigue interactions and the limited sample size in this study, high-temperature fatigue tests with stress-controlled dwell times should be performed more often to emulate service-like creep phases and be followed up microscopically. A well-founded mechanistic and microstructure-based understanding of possibly deviating damage mechanisms for long creep or relaxation phases could thereby i) verify the comparability of results from RF experiments to simplified or actual service-like creep-fatigue conditions or ii) show limits (thresholds) of

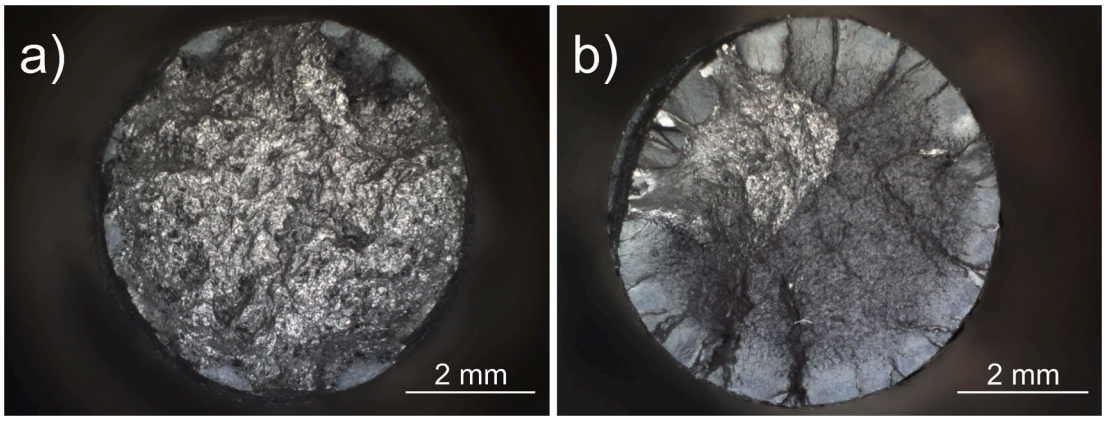

Fig. 12. Fracture surfaces of test pieces for (a) SLC and (b) SLR experiment (optical bright-field microscopy).

transferability and thus iii) enable solid models and extrapolation techniques for long-term creep and relaxation fatigue.

For a rough estimate of creep-fatigue interactions for short DTs, RF tests remain an appropriate and efficient tool, provided that possible restrictions on limited transferability are considered during analysis and interpretation, especially regarding anticipated creep mechanisms and environmental effects. Furthermore, since high viscoplastic deformations can be generated in concise time increments using relaxation dwells, RF tests are particularly suitable for the first exploration of larger parameter spaces (e.g., concerning Coffin-Manson relations, different test temperatures, strain rates, phase angles in TMF, etc.).

Finally, it should be noted that – notwithstanding presumably different creep mechanisms in long DTs at low constant stresses or strains – creep (relaxation)-fatigue testing remains indispensable for the assessment of the mechanical behavior of materials, such as 9–12 %Cr steels subjected to high-temperature, load-flexible service conditions: On the one hand, phases of constant operation reduce cyclic fatigue life enormously compared to continuous tests (Fig. 13). Given the limited sample size in this study, it is indicated that the SL tests cause significant lifetime reductions of about 85 % compared to LCF tests and up to 33 % compared to "classical" RF tests. On the other hand, cyclic loading drastically reduces creep resistance and creep rupture time. For instance, the SLC specimen tested in this study was subjected to a transient creep loading under constant stresses of 121–133 MPa (cf. Fig. 8b) during SSOs of 30 min each at 620 °C for 1370 cycles. That is, failure occurred after 685 h of pure creep loading (or after about 860 h of total creep-fatigue loading). Thus, compared to the standard specifications of P92, like the 10,000 h creep rupture strength of 126 MPa at 620 °C [47], the actual fracture time of the SLC test was reduced to less than 10 % of this requirement for a comparable stress level.

The observed impacts on both fatigue life and creep life, underline that combined creep-fatigue loading must be regarded as drastically more detrimental than pure creep or pure fatigue loadings for tempered martensite-ferritic steels. Thus, a linear damage accumulation cannot be assumed. Recently, Riedel et al. [48] revisited this phenomenon and suggested a dedicated lifetime model for grade P92 material based on their test data. The authors point out that their findings are in good agreement with the creep-fatigue limits reported in power plant design codes for the preceding grade P91 steel. These codes suggest that early failure at about 10 % (or less) of the pure fatigue or pure creep life must be expected if only 10 % life consumption of the respective other was accumulated before in combined cycles.

A corresponding quantification of the lifetime effects of the current combined loads would be beyond the scope of the present study with its limited experimental database. It is, though, worth noting that the initially surprising result of nearly similar cycles to failure in our SLR and SLC tests (Fig. 13), despite their obviously different failure mechanisms with clear "fatigue" and "creep" based character, supports the abovementioned view of pronounced creep-fatigue interaction in P92 on a qualitative level: The combination of both load types (and their related damage processes) resulted in an early fracture, independent of the dominant part of loading. However, such simplified interpretations tend to hamper a fundamental understanding of the underlying mechanisms. Only an extended database, including, e.g., variable amplitude loading and the related question of load sequence effects, as well as a sound microscopy-based mechanistic understanding, will allow to fully elucidate the reaction of P92 to different combined loading scenarios.

4. Conclusions

The creep-fatigue behavior of tempered-martensite ferritic steel grade P92 at 620 °C was investigated. The complex mechanical loading for all tests comprised: i) fatigue loading at a low total strain amplitude ($\varepsilon_{t,a} = \pm 0.2\%$) in the region of the material's high-temperature elastic–plastic transition, ii) symmetrical three-minute strain-controlled dwells at ε_{max} and ε_{min}, and iii) 30-minute dwells (SSOs) at $\varepsilon_{start,SSO} = 0$ in the nominally elastic regime to mimic steady-state operation. These SSO periods were either conducted in strain-control to enable long-term stress relaxation (service-like relaxation test, *SLR*) or in stress-control to facilitate true creep (service-like creep test, *SLC*). Based on the mechanical analysis, first-order approximations of the expected creep mechanisms, and optical microscopy, the following conclusions are drawn:

- The magnitude of creep strain evolving during individual long-term stress- or strain-controlled SSOs is only comparable for a few seconds in an early primary creep stage. While constant stress in *SLC* causes a continuous increase in creep strain with time, the continuous stress relaxation under constant strain in *SLR* is accompanied by a simultaneous reduction in the driving force for creep processes. This study hints at a continuous shift from stress-controlled viscoplastic creep processes to time- and diffusion-controlled processes at the end of an SSO in the *SLR* test.
- Because the creep behavior is already fundamentally different within the 30-minute SSOs of both test types, the dwell design also influences the deformation processes during identical subsequent transient load shifts and thus alters the global cyclic softening behavior: Compared to a classical relaxation fatigue (RF) test with three-minute dwells at ε_{max} and ε_{min}, retarded and accelerated cyclic softening are observed for *SLC* and *SLR*, respectively.
- The impact of the combined creep-fatigue loading is not limited to the deformation and softening processes. In the *SLC* and *SLR* tests, fatigue lives were reduced by 33 % and 85 % compared to the corresponding RF and LCF tests, respectively, indicating that different damage mechanisms interact in this case and promote the accumulation of defects and the formation of cracks.
- The development of significant creep strain during individual SSOs in the *SLC* test reduces the effective strains that must be applied in subsequent ramps toward ε_{max}. This leads to most of the viscoplastic deformation being generated during the SSOs, pronounced creep damage with creep cavitation, and crack initiation in the bulk and possibly intergranular crack propagation. In contrast, multiple fatigue cracks form at the lateral specimen surface in the *SLR* test that oxidate particularly during the long-term high-temperature SSO periods and accelerate transgranular crack growth.
- These apparent mechanistic differences partly question the common approach of a purely strain-controlled test design for the characterization of creep-fatigue interactions. Depending on the intended load level and dwell time duration, the transferability of strain-controlled relaxation periods to stress-controlled creep periods in fatigue testing should therefore be critically examined during the design of experiments. Additional studies focusing on mechanistic microstructural comparisons between long-term relaxation and creep could help prove or disprove the hypotheses put forward in this study. However, for a rough estimate of creep-fatigue interactions and fatigue life, RF tests with short DTs are an appropriate and efficient tool, provided that possible restrictions on limited transferability are considered during analysis and interpretation.

Declaration of Competing Interest

The authors declare that they have no known competing financial interests or personal relationships that could have appeared to influence the work reported in this paper.

Data availability

The authors have attached to this submission a manuscript entitled "Experimental Data from Service-Like Creep-Fatigue Experiments on Grade P92 Steel" to be submitted to *Data in Brief*. We wish to share stress, strain, temperature, and time data of SLC, SLR, and RF tests therein.

Acknowledgements

This research was funded by the German Federal Ministry of Education and Research under grant number 03SF0474. The material was provided by the company Vallourec. The authors also wish to thank Ole Kahlcke and Patrick Uhlemann for their experimental support.

References

[1] Masuyama F. History of power plants and progress in heat resistant steels. ISIJ Int 2001;41(6):612–25.
[2] Viswanathan V, Purgert R, Rawls P. Coal-fired power materials. Adv Mater Processes 2008, Aug;166(8):47–9.
[3] Zhang Z, Hu Z, Schmauder S. Low-cycle fatigue properties of P92 ferritic-martensitic steel at elevated temperature. J Mater Eng Perform 2016;25(4):1650–62.
[4] Fournier B, Sauzay M, Pineau A. Micromechanical model of the high temperature cyclic behavior of 9–12%Cr martensitic steels. Int J Plast 2011;27(11):1803–16.
[5] Pineau A, Antolovich SD. High temperature fatigue: behaviour of three typical classes of structural materials. Mater High Temp 2015;32(3):298–317.
[6] Pesicka J, et al. The evolution of dislocation density during heat treatment and creep of tempered martensite ferritic steels. Acta Mater 2003;51(16):4847–62.
[7] Klueh RL. Elevated temperature ferritic and martensitic steels and their application to future nuclear reactors. Int Mater Rev 2005;50(5):287–310.
[8] Shibli A, Gostling J, Starr F. Damage to power plants due to cycling. EPRI; 2001.
[9] Viswanathan R, Bakker W. Materials for ultrasupercritical coal power plants-boiler materials: Part 1. J Mater Eng Perform 2001;10(1):81–95.
[10] Farragher TP, et al. Development of life assessment procedures for power plant headers operated under flexible loading scenarios. Int J Fatigue 2013;49:50–61.
[11] Shibli A, Ford J. Damage to coal power plants due to cyclic operation. In: Shibli A, editor. Coal power plant materials and life assessment. Woodhead Publishing; 2014. p. 333–57.
[12] Cui L, Wang P. Two lifetime estimation models for steam turbine components under thermomechanical creep–fatigue loading. Int J Fatigue 2014;59:129–36.
[13] Wang XW, et al. Characterization of low cycle fatigue performance of new ferritic P92 steel at high temperature: effect of strain amplitude. Steel Res Int 2015;86(9):1046–55.
[14] Zhang Z, Hu Z, Fan L. Low cycle fatigue behavior and cyclic softening of P92 ferritic-martensitic steel. J Iron Steel Res Int 2015;22(6):534–42.
[15] Saad AA et al. Cyclic softening behaviour of a P91 steel under low cycle fatigue at high temperature. In: 11th International conference on the mechanical behavior of materials (Icm11); 2011. p. 1103–8.
[16] Mishnev R, Dudova N, Kaibyshev R. Low cycle fatigue behavior of a 10Cr-2W-Mo-3Co-NbV steel. Int J Fatigue 2016;83:344–55.
[17] Shankar V, et al. Low cycle fatigue behavior and microstructural evolution of modified 9Cr-1Mo ferritic steel. Mater Sci Eng, A 2006;437(2):413–22.
[18] Fournier B, Sauzay M, Renault A. Microstructural evolutions and cyclic softening of 9%Cr martensitic steels. J Nucl Mater 2009:71–4.
[19] Pan XM, et al. Thermal-mechanical fatigue behavior and lifetime prediction of P92 steel with different phase angles. Int J Fatigue 2018;109:126–36.
[20] Mannan SL, Valsan M. High-temperature low cycle fatigue, creep-fatigue and thermomechanical fatigue of steels and their welds. Int J Mech Sci 2006;48(2):160–75.
[21] Jürgens M, et al. Low cycle fatigue and relaxation performance of ferritic-martensitic grade P92 steel. Metals 2019;9(99).
[22] Nagesha A, et al. Isothermal and thermomechanical fatigue studies on a modified 9Cr-1Mo ferritic martensitic steel. Mater Sci Eng, A 2012;554:95–104.
[23] Barrett RA, et al. Thermomechanical fatigue in 9–12Cr steels: life prediction models and the effect of tensile dwell periods. Int J Fatigue 2019;126:335–45.
[24] Shankar V, et al. Low cycle fatigue and thermo-mechanical fatigue behavior of modified 9Cr-1Mo ferritic steel at elevated temperatures. J Nucl Mater 2012;420(1–3):23–30.
[25] Chang L, et al. Thermal-mechanical fatigue behaviour and life prediction of P92 steel, including average temperature and dwell effects. J Mater Res Technol 2020;9(1):819–37.
[26] Wen JB, et al. Effect of temperature range on thermal-mechanical fatigue properties of P92 steel and fatigue life prediction with a new cyclic softening model. Int J Fatigue 2019;129.
[27] Jürgens M, et al. The effect of dwell times on the thermomechanical fatigue life performance of grade P92 steel at intermediate and low strain amplitudes. Mater Sci Eng, A 2021;805:140593.
[28] Fournier B, et al. Creep-fatigue-oxidation interactions in a 9Cr-1Mo martensitic steel. Part 1: effect of tensile holding period on fatigue lifetime. Int J Fatigue 2008;30(4):649–62.
[29] Fournier B, et al. Creep-fatigue-oxidation interactions in a 9Cr-1Mo martensitic steel. Part II: effect of compressive holding period on fatigue lifetime. Int J Fatigue 2008;30(4):663–76.
[30] Zhang T, et al. P92 steel creep-fatigue interaction responses under hybrid stress-strain controlled loading and a life prediction model. Int J Fatigue 2020;140:105837.
[31] Fournier B, et al. Creep–fatigue–oxidation interactions in a 9Cr–1Mo martensitic steel. Part I: effect of tensile holding period on fatigue lifetime. Int J Fatigue 2008;30(4):649–62.
[32] Fournier B, et al. Analysis of the hysteresis loops of a martensitic steel: Part II: study of the influence of creep and stress relaxation holding times on cyclic behaviour. Mater Sci Eng, A 2006;437(2):197–211.
[33] Cui L, et al. The influence of temperature transients on the lifetime of modern high-chromium rotor steel under service-type loading. Mater Sci Eng, A 2013;560:767–80.
[34] Goswami T, Hanninen H. Dwell effects on high temperature fatigue damage mechanisms: Part II. Mater Des 2001;22(3):217–36.
[35] Scholz A, Berger C. Deformation and life assessment of high temperature materials under creep fatigue loading. Materialwiss Werkstofftech 2005;36(11):722–30.
[36] Liu Z, et al. Creep-fatigue interaction and damage behavior in 9–12%Cr steel under stress-controlled cycling at elevated temperature: effects of holding time and loading rate. Int J Fatigue 2022;156:106684.
[37] Zong Y, et al. Investigation on high temperature short-term creep and stress relaxation of titanium alloy. Mater Sci Eng, A 2015;620:172–80.
[38] Guo J, et al. Prediction of stress relaxation from creep data in terms of average creep rate. J Strain Anal Eng Des 2014;50(1):15–24.
[39] Khayatzadeh S, et al. Creep deformation and stress relaxation of a martensitic P92 steel at 650°C. Eng Fract Mech 2017;175:57–71.
[40] Kassner ME. Fundamentals of creep in metals and alloys. 3rd edn. Boston: Butterworth-Heinemann; 2015.
[41] Kalyanasundaram V, Holdsworth SR. Prediction of forward creep behaviour from stress relaxation data for a 10 % Cr steel at 600 °C. Trans Indian Inst Met 2016;69(2):573–8.
[42] Frost HJ, Ashby MF. Deformation-mechanism maps for pure iron, two austenitic stainless steels, and a low-alloy ferritic steel. In: Jaffee RI, Wilcox BA, editors. Fundamental aspects of structural alloy design. Boston, MA: Springer US; 1977. p. 27–65.
[43] Kloc L, Sklenička V. Transition from power-law to viscous creep behaviour of p-91 type heat-resistant steel. Mater Sci Eng, A 1997;234–236:962–5.
[44] Yamamoto Y, Ortolani M. Micrograin structure evolution associated with grain boundary characteristics in grade 91 steel during long-term creep exposure. Mater Sci Eng, A 2021;826:141993.
[45] Panwisawas C, et al. The contrasting roles of creep and stress relaxation in the time-dependent deformation during in-situ cooling of a nickel-base single crystal superalloy. Sci Rep 2017;7(1):11145.
[46] Wang H, et al. Studying the effect of stress relaxation and creep on lattice strain evolution of stainless steel under tension. Acta Mater 2013;61(4):1179–88.
[47] DIN EN 10216-2:2020-04. Seamless steel tubes for pressure purposes - technical delivery conditions - Part 2: non-alloy and alloy steel tubes with specified elevated temperature properties; German version EN 10216-2:2013+A1:2019. Berlin, Germany: Beuth Publishing; 2020.
[48] Riedel H, Maier G, Oesterlin H. A lifetime model for creep-fatigue interaction with applications to the creep resistant steel P92. Int J Fatigue 2021;150:106308.